KURENAI
Kyoto University Research Information Repository

KYOTO UNIVERSITY

Title	S-wave impedance measurements of the uppermost material in surface ground layers: Vertical load excitation on a circular disk
Author(s)	Goto, Hiroyuki; Tanaka, Nobuaki; Sawada, Sumio; Inatani, Hideki
Citation	Soils and Foundations (2015), 55(5): 1282-1292
Issue Date	2015-10
URL	http://hdl.handle.net/2433/203020
Right	© 2015. This manuscript version is made available under the CC-BY-NC-ND 4.0 license http://creativecommons.org/licenses/by-nc-nd/4.0/; The full-text file will be made open to the public on 1 October 2017 in accordance with publisher's 'Terms and Conditions for Self-Archiving'.; This is not the published version. Please cite only the published version.
Type	Journal Article
Textversion	author

Kyoto University

S-wave impedance measurements of the uppermost material in surface ground layers: vertical load excitation on a circular disk

Hiroyuki Goto[a,*], Nobuaki Tanaka[b], Sumio Sawada[a], Hideki Inatani[c]

[a]*Disaster Prevention Research Institute, Kyoto University, Gokaho, Uji, Kyoto 611-0011, Japan*
[b]*Chemical Grouting Co., Ltd., Toranomon, Minato Ward, Tokyo 105-0001, Japan*
[c]*Katsujima Co., Ltd., Shiratori, Katsushika Ward, Tokyo 125-0063, Japan*

Abstract

S-wave impedance is one of the most effective parameters used to study the ground motion amplification of soil deposits. We propose a new approach to measure the S-wave impedance of the uppermost material in surface ground layers. First, a circular disk is set on the ground surface, and it is vertically loaded by sinusoidal wave excitation. When the time series of the loading velocity is synchronized with the reaction force, the ratio of the reaction force to the loading velocity is proportional to the S-wave impedance. We then estimate the proportionality coefficient from numerical experiments and check its accuracy. The measurement error is estimated to be within 1% for the homogeneous half-space case. We also discuss the applicability of this new approach and its limitations on the bases of numerical experiments for inhomogeneous media: a two-layered medium and a one-dimensional (1-D) random medium. The proposed approach is effective for both cases if we select the appropriate circular disk size.

Keywords: S-wave impedance, Elastic wave exploration, Numerical experiment (IGC: C02, E08, G08)

---

*Corresponding author.
E-mail address: goto@catfish.dpri.kyoto-u.ac.jp (H. Goto).

1. Introduction

Evaluating the risk of on earthquake disasters is one of the important issues in geotechnical engineering. In one example, the liquefaction potential for a future great earthquake has been assessed by each local goverment in Japan. The potential is conventionally estimated from the value of F_L, which is the factor of safety corresponding to liquefaction defined by R/L, where R is the dynamic shear strength, and L is the maximum shear stress. The F_L values at actual liquefaction sites have been well discussed for the 2011 off the Pacific coast of Tohoku earthquake (e.g., Unjoh et al., 2012; Yasuda et al., 2012; Towhata et al., 2014). In order to estimate the relative potential of liquefaction via the F_L values, the maximum shear stress L acting on the soil column is required. L is originally calculated from the acceleration on the ground surface (Seed and Idriss, 1971), and now other ground motion indexes are also applied.

Thus, it is an essential procedure to quantify the ground motion amplification. In addition, the amplification due to the soil ground deposits directly caused severe damage to geotechnical structures during the 2011 off the Pacific coast of Tohoku earthquake (e.g., Mori et al., 2012; Hata et al., 2014; Sugano et al., 2014). Therefore, the amplification has been well considered, even in geotechnical engineering.

Several approaches have been proposed to quantify the amplification. Some of them have already been introduced into real-time systems that can estimate the impact of earthquake disasters (Wald et al., 2010). These approaches are based on simple factors that classify the ground (Bouzorgnia and Bertero, 2004) via the averaged shear wave velocity, surface geology, geotechnical data, etc. Recently, Vs_{30}, the averaged shear wave velocity to a 30 m depth, has been widely adopted for site classifications (Borcherdt, 1994). Geomorphologic classifications (Wakamatsu and Matsuoka, 2006) and topographic data (Wald and Allen, 2007; Allen and Wald, 2009; Thompson et al., 2014) are used to evaluate Vs_{30} at sites where detailed velocity profiles are not available.

Some researchers, however, argue that Vs_{30} is not a significant parameter to

model the site amplification (Castellaro et al., 2008; Lee and Trifunac, 2010). However, the ratio of the S-wave impedance, that is, the product of S-wave velocity and density, was originally proposed to be the index to quantify the amplification. Joyner et al. (1981) pointed out that the amplification may be explained by the square root of the impedance ratio of rock to soil sites. Their idea has, unfortunately, not been readily accepted because they neglect the energy losses due to reflection at the material interface, which is essential to observe the resonance frequency of the surface ground. In recent research, the S-wave impedance was revived by Goto et al. (2011) in their analysis of the normalized energy density (NED). The NED is a single value model of the site amplification, but it integrates the frequency contents of the transfer function for the surface layer. The NED and average of the amplification are strongly correlated, which has been proven mathematically and numerically. In applications, the total damping in the surface ground can be directly estimated from the loss of the NED (Goto et al., 2013). In order to evaluate the NED at a particular site, the S-wave impedance of the uppermost surface layer is an essential physical parameter to obtain, and it has to be measured by in situ field tests.

The S-wave impedance of the surface layer is also an important factor that is used to model soil-structure interactions. As reviewed by Kausel (2010), a large amount of research has focused on these types of interactions, which have been reported since the end of the 19th century. Gazetas (1991) summarized the approximate formulas of the dynamic stiffness and dashpot coefficient for various types of foundations. In his chart, the dashpot coefficient, which physically represents the radiation damping, is a function of the material impedance of the surface ground (Gazetas and Dobry, 1984; Gazetas and Tassoulas, 1987). Because the impedance corresponds to the S-wave velocity or Lysmer's analog wave velocity, depending on the response directions, the S-wave impedance is a key parameter to model the dashpot coefficient of the foundations (e.g., Wolf and Somaini, 1986; Wolf, 1997; Gerolymos and Gazetas, 2006).

The S-wave impedance at the actual site has been estimated from the product of the measured S-wave velocity and density. The S-wave velocity profile

is measured by various types of elastic wave explorations (Boore, 2006) such as PS logging, refraction surveys, reflection surveys (e.g., Allen, 1980; Yokokura, 1995), surface wave surveys (Park et al., 1999), and microtremor array observations (e.g., Aki, 1957, 1965; Okada, 2003; Goto et al., 2009). The density profile is measured from undisturbed soil samples or by density logging (e.g., Jia et al., 2013). Although each technique has been well established, measurement errors and uncertainties still remain (e.g., Liu et al., 2000; Boore and Thompson, 2007). This may cause error propagation during estimation of the S-wave impedance. Thus, it is better to measure the S-wave impedance directly without the product.

Recently, direct estimation techniques of the material impedance for the subsurface structure have been developed in the field of exploration geophysics (Connolly, 1999; Whitcombe, 2002; Lu and McMechan, 2004). These techniques focus on the angle-dependent reflections from the material interface, and the dependence is estimated from the variation. These approaches are attractive, but they require several seismic records with a variety of angles. Because the body waves tend to travel vertically through the surface layers, a sufficient variation in the angles may not be available.

In this study, we propose a new technique to measure the S-wave impedance on the uppermost surface layer. We focus on the dynamic response of a rigid circular disk, which is placed on a target ground surface. The relations of the S-wave impedance and the ratio of the reaction force to the velocity at a synchronized frequency are described, and we then propose a procedure to estimate the S-wave impedance. Lastly, we present the results from two types of numerical experiments and verify the proposed technicque.

2. Robertson's solution

2.1. Analytical solution for the dynamic response of a circular disk

A rigid circular disk is placed on the free surface of a homogeneous half-space medium, and it is vertically loaded by sinusoidal wave excitation. Let a be the

4

disk radius. The cylindrical coordinate system is adopted, as shown in Fig. 1. Robertson (1966) analytically solved the dynamic response of the circular disk under the following boundary conditions:

$$u_z(r, 0, \omega) = u(\omega) \qquad \text{for } r \leq a, \tag{1}$$

$$\sigma_{zz}(r, 0, \omega) = 0 \qquad \text{for } a < r, \tag{2}$$

$$\sigma_{rz}(r, 0, \omega) = 0 \qquad \text{for } 0 \leq r, \tag{3}$$

where u_r and u_z and σ_{rr}, σ_{rz}, and σ_{zz} are the displacement and stress components, respectively. $u(\omega)$ denotes a forced displacement applied vertically to the disk, and its angular frequency is ω.

The reaction force acting vertically on the disk $P_z(\omega)$ was represented as follows:

$$\frac{P_z(\omega)}{\pi a^2} = \frac{4\mu u(\omega)}{\pi a(1 - \nu)}(p_1(\omega) - ip_2(\omega)), \tag{4}$$

where μ and ν are the shear modulus and Poisson ratio of the medium, respectively. i is the imaginary unit. $p_1(\omega)$ and $p_2(\omega)$ are real functions, which are represented by the series of $a\omega/\beta$:

$$p_1(\omega) = 1 + \frac{1}{3\pi^2}(2\pi I_2 - 3I_1^2)\left(\frac{a\omega}{\beta}\right)^2$$
$$+ \frac{1}{60\pi^4}(60I_1^4 - 40\pi^3 I_4 + 28\pi^2 I_1 I_3 + 33\pi^2 I_2^2 - 120\pi I_1^2 I_2)\left(\frac{a\omega}{\beta}\right)^4 + \cdots, \tag{5}$$

$$p_2(\omega) = \frac{1}{\pi} I_1\left(\frac{a\omega}{\beta}\right) - \frac{1}{3\pi^3}(\pi^2 I_3 - 4\pi I_1 I_2 + 3I_1^3)\left(\frac{a\omega}{\beta}\right)^3 + \cdots, \tag{6}$$

where β is the S-wave velocity. I_n is a real coefficient that only depends on ν. By substituting $\omega = 0$, $p_2(\omega)$ vanishes, and the reaction force is proportional to the displacement. In this case, Eq. (4) is identical to the static solution (Boussinesq, 1885; Lamb, 1902).

2.2. Implication and limitation of Robertson's solution

For a small angular frequency, the series in Eqs. (5)–(6) can be approximated by a small number of terms. Let $\tilde{p}_1(\omega)$ and $\tilde{p}_2(\omega)$ be the low-order approxima-

tions of $p_1(\omega)$ and $p_2(\omega)$ so that

$$\tilde{p}_1(\omega) = 1 + \frac{1}{3\pi^2}(2\pi I_2 - 3I_1^2)\left(\frac{a\omega}{\beta}\right)^2, \tag{7}$$

$$\tilde{p}_2(\omega) = \frac{1}{\pi}I_1\left(\frac{a\omega}{\beta}\right). \tag{8}$$

As ω increases, $\tilde{p}_1(\omega)$ monotonically decreases because $2\pi I_2 < 3I_1^2$, and $\tilde{p}_2(\omega)$ monotonically increases. Therefore, the root of $\tilde{p}_1(\omega) = 0$, $\tilde{\omega}$, exists. By substituting $\tilde{\omega}$ into Eq. (4), the reaction force is represented as follows:

$$\begin{aligned}
\frac{P_z(\tilde{\omega})}{\pi a^2} &= \frac{4\mu u(\tilde{\omega})}{\pi a(1-\nu)}(\tilde{p}_1(\tilde{\omega}) - i\tilde{p}_2(\tilde{\omega})) \\
&= \frac{4\mu u(\tilde{\omega})}{\pi a(1-\nu)}\left(-\frac{iI_1}{\pi}\frac{a\tilde{\omega}}{\beta}\right) \\
&= \frac{4I_1\rho\beta\dot{u}(\tilde{\omega})}{\pi^2(1-\nu)} = I_0\rho\beta\dot{u}(\tilde{\omega}),
\end{aligned} \tag{9}$$

where ρ is the density. $\dot{u}(\tilde{\omega})$ is the disk velocity that is defined by $\dot{u}(\tilde{\omega}) \equiv -i\tilde{\omega}u(\tilde{\omega})$. I_0 is a real coefficient that only depends on ν.

Equation (9) suggests that the reaction force is proportional to the disk velocity when the reaction force is synchronized with the disk velocity. The S-wave impedance $\rho\beta$ explicitly appears in the proportional coefficient. This relation implies that it is possible to measure the S-wave impedance by using the ratio of the reaction force and the disk velocity at the synchronized frequency.

However, Robertson's solution and the above approximation involve several queries that need to be generalized for the measurement of the S-wave impedance for the actual ground.

2.2.1. Dependency on the Poisson ratio

The coefficient I_0 depends on ν, which is also a material parameter. If we want to obtain accurate values of I_0, ν for the target material is required.

2.2.2. Stress-free condition beneath the disk

Equation (9) is based on Robertson's solution, which is solved under the boundary condition in Eqs. (1)–(3). The stress-free condition beneath the disk

(Eq. (3)) requires frictionless slip between the disk and the surface of the medium. This may not be a realistic condition for the actual system.

2.2.3. Low-order approximation of the series

Although the S-wave impedance explicitly appears in the proportional coefficient in Eq. (9), the derivation is based on the low-order approximations of the series (Eqs. (5)–(6)) by assuming a small angular frequency. However, the observed reaction force involves all terms of the series. It is required to check for the existence of the synchronized frequency, and the relation between the reaction force and the disk velocity is obtained by considering the contribution from the high-order terms of the series.

2.2.4. Heterogeneity of the surface ground

Robertson's solution is for a homogeneous half-space medium. However, the actual surface ground consists of more complicated structures such as layered structures with fluctuating material parameters.

3. Numerical simulation of the dynamic response in a homogeneous half-space medium

Instead of Robertson's solution, we numerically simulate the dynamic response of the rigid circular disk in a homogeneous half-space medium and discuss the relation between the reaction force and the disk velocity.

3.1. Simulation method

The equations of motion for the cylindrical coordinate system with axial symmetry and the constitutive models for linear elasticity are applied. These include

$$\rho \ddot{u}_r = \frac{\partial \sigma_{rr}}{\partial r} + \frac{\sigma_{rr}}{r} + \frac{\partial \sigma_{rz}}{\partial z} - \frac{\sigma_{\theta\theta}}{r}, \tag{10}$$

$$\rho \ddot{u}_z = \frac{\partial \sigma_{rz}}{\partial r} + \frac{\sigma_{rz}}{r} + \frac{\partial \sigma_{zz}}{\partial z}, \tag{11}$$

$$\sigma_{rr} = (\lambda + 2\mu)\frac{\partial u_r}{\partial r} + \lambda\frac{u_r}{r} + \lambda\frac{\partial u_z}{\partial z}, \tag{12}$$

$$\sigma_{\theta\theta} = \lambda\frac{\partial u_r}{\partial r} + (\lambda + 2\mu)\frac{u_r}{r} + \lambda\frac{\partial u_z}{\partial z}, \tag{13}$$

$$\sigma_{zz} = \lambda\frac{\partial u_r}{\partial r} + \lambda\frac{u_r}{r} + (\lambda + 2\mu)\frac{\partial u_z}{\partial z}, \tag{14}$$

$$\sigma_{rz} = \mu\left(\frac{\partial u_r}{\partial z} + \frac{\partial u_z}{\partial r}\right). \tag{15}$$

In the numerical simulation, we constrain the radial displacement beneath the disk. The boundary conditions for the z-component are the same as those with Robertson's solution (Eqs. (1)–(2)), whereas we apply the following condition for the r-component:

$$u_r(r, 0, \omega) = 0 \qquad\qquad \text{for } r \leq a, \tag{16}$$

$$\sigma_{rz}(r, 0, \omega) = 0 \qquad\qquad \text{for } a < r. \tag{17}$$

The finite element method is adopted to solve the above boundary value problem. We adopt a rectangular four-node isoparametric element. Beneath the disk ($r \leq a$), 50 square elements are allocated in the horizontal direction. The edge size of the elements is completely uniform in the vertical direction, whereas it is uniform within twice the size of the disk radius and gradually enlarged by a scale factor of 1.015 until the end of the entire domain. We set the size of the entire domain so that the reflection waves from the artificial boundary will not return to the disk, and then, we apply 300×300 elements to represent the entire domain, which is $27.4a \times 12.0a$. One-dimensional (1-D) nonreflecting boundary conditions are also allocated at the artificial boundaries to minimize the effect of the reflection waves, specifically, on the side and bottom edges of the domain, as shown in Fig. 2.

The centered difference scheme is adopted to solve the differential equation associated with time. The time step Δt is set to be $\Delta x_{\min} C / \alpha_{\max}$, where $\Delta x_{\min}$ is the minimum size of an element edge, $\alpha_{\max}$ is the maximum value of the P-wave velocity, and C is a coefficient that represents the Courant–Friedrichs–Lewy (CFL) condition. In this case, $\Delta x_{\min}$ is equal to $a/50 = 0.02\,\text{m}$. If we select $C = 0.5$ to satsify the CFL condition, the time steps are 0.01 divided by

the P-wave velocity.

To model the dynamic load on the rigid disk, the forced displacement $(u(\omega), 0)$ is explicitly applied to the nodes located in $r \leq a$ on the top edge. The reaction force is calculated by summing the nodal forces to keep the forced displacement beneath the disk.

At the beginning of excitation, the amplitude linearly increases to $0.01\,\mathrm{m}$ after two cycles of oscillation and remains constant for 15 cycles. The cross correlation between the disk velocity and the reaction force is calculated during the elapsed time of the 2–15 cycles,

$$g(t) = \int_{2/f_p}^{15/f_p} \dot{u}(\tau) P_z(\tau + t) d\tau, \tag{18}$$

where f_p is excitation frequency. Let $t_{\max}$ be the time shift to obtain the maxmum value of $g(t)$ within $-0.5 f_p < t < 0.5 f_p$. Then, the phase difference is estimated from $360\, t_{\max} f_p$.

3.2. Results

The physical parameters of a homogeneous half-space medium, the S-wave velocity, the density, and the Poisson ratio are listed in Table 1. We simulated all of the combination cases (140 cases). The disk radius is $a = 1.0\,\mathrm{m}$. The excitation frequencies are in the range from $\beta/20a$ to $\beta/2a\,\mathrm{Hz}$ with an interval of $\beta/40a\,\mathrm{Hz}$, e.g., 25 to 250 Hz with an interval of 12.5 Hz for the $\beta = 500\,\mathrm{m/s}$ cases. The range is determined from the results of a few sample simulations to obtain a significant relation with the phase difference, as described later. Because the maximum frequency is insufficient to find the synchronized frequency for the $\nu = 0.40$ and 0.41, it is enlarged to $\beta/a\,\mathrm{Hz}$.

Figure 3 shows the time series of the averaged reaction pressure and disk velocity for $\beta = 200\,\mathrm{m/s}$, $\rho = 1500\,\mathrm{kg/m}^3$, and $\nu = 0.45$ simulated for the excitation frequencies of 20 Hz and 75 Hz. The averaged reaction pressure is defined by $P_z/\pi a^2$. A large phase difference between the averaged reaction pressure and the disk velocity was observed for the 20 Hz case, whereas the phase difference was almost zero for the 75 Hz case. This implies that the phase

9

difference depends on the excitation frequency. Note that the numerical results for the half-space case are controlled by the normalized frequency, $a\omega/\beta$. The frequency range is scaled to be lower if a larger disk size is adopted.

Figure 4 shows the phase differences between the averaged reaction pressure and the disk velocity for each excitation frequency. We also add a phase difference of $90°$ at $0\,\text{Hz}$ because the static load must be propotional to the disk displacement that is at a phase difference of $90°$ from the velocity. The phase differences monotonically decrease and cross the zero axis. The frequency crossing the zero axis was estimated as $83.8\,\text{Hz}$, and this is named the synchronized frequency hereinafter. Figure 4 also shows the amplitude ratio of the averaged reaction pressure to the disk velocity. We focus on the ratio at the synchronized frequency, which is named the measured ratio hereinafter, because Eq. (9) implies that the ratio is proportional to the S-wave impedance at the synchronized frequency. In this case, the measured ratio is $6.84 \times 10^5\,\text{kg/sm}^2$.

The coefficients I_0 and I_1 in Eq. (9) are functions of the Poisson ratio. The values for this case are 1.859 and 2.523, respectively. If the result satisfies Eq. (9), the measured ratio divided by I_0 must be equal to the S-wave impedance of the medium, which is equal to $3.00 \times 10^5\,\text{kg/sm}^2$. However, this value is $22\,\%$ larger than the true value. The overestimation is caused by the limitation of Eq. (9), as mentioned in Section 2.2. One piece of evidence is the value of $a\tilde{\omega}/\beta$, which was calculated to be 2.63. It does not satisfy the assumption that the higher-order terms in Eqs. (5)–(6) can be neglected. This means that the measured ratio is not ensured to be proportional to the S-wave impedance. Therefore, we had to check the relation between the measured ratio and the material S-wave impedance.

We define a new coefficient $\tilde{I}_0$ by the ratio of the measured ratio to the material S-wave impedance. Figure 5 shows the values of $\tilde{I}_0$ for all simulated cases. As a reference, I_0 for $\nu = 0.50$ for Robertson's solution is also plotted in the figure. The results indicate that the coefficient, except for the case of $\nu = 0.40$, is independent of the S-wave velocity, Poisson ratio, and density. I_0 originally depends on the Poisson ratio, whereas the dependence disappears in

10

the results from the numerical experiments.

In order to discuss the reason why the Poisson ratio dependency disappears for $\tilde{I}_0$, we perform additional numerical simulations. The simulations allow frictionless sliding between the disk and the ground surface, which is the same boundary conditions with Robertson's solution. Figure 6 shows the results obtained from the simulations for $\nu = 0.45, 0.48$, and 0.49, which are plotted with I_0 from Robertson (1966). If the low-order approximation (Section 2.2.3) is available, the results agree with I_0. However, the ratios of the measured ratio to the material S-wave impedance are larger than I_0. The values of $a\tilde{\omega}/\beta$ are in the range of 3.10–3.13, 2.56–2.58, and 2.46–2.49 for $\nu = 0.45, 0.48$, and 0.49, respectively, which do not satisfy the low-order assumption. This implies that the discrepancy between the obtained results and I_0 is explainable by rejection of the low-order approximation. On the other hand, the Poisson ratio dependency still remains for the frictionless cases because the results for $\nu = 0.49$ are larger than the others. We interpret that the reason for this is the difference of the constraint beneath the disk because the constraint of horizontal sliding may restrict the Poisson effect.

The results in Fig. 5 also indicate that the measured ratio is proportional to the S-wave impedance, and its proportionality coefficient can be represented by a unique constant $\tilde{I}_0$. The average value of $\tilde{I}_0$ among the results for $\nu = 0.45, 0.48$, and 0.49 is 2.2788. We checked the applicability of $\tilde{I}_0 = 2.2788$ for the other cases. Figure 7 shows a comparison between the estimated S-wave impedance from the measured ratio divided by $\tilde{I}_0 = 2.2788$ and the material true values. The estimated S-wave impedances are almost equal to the true ones, except for $\nu = 0.40$. The standard deviation of the estimation error for $\nu \geq 0.41$ is 0.99 %, which is quite small to measure the S-wave impedance. As mentioned in Section 2.2, the original coefficient I_0 depends on the Poisson ratio. However, the results indicate we can apply $\tilde{I}_0 = 2.2788$ independent of the Poisson ratio if the material is in the range $\nu \geq 0.41$. This is an efficient property of the proposed technique because the detailed values of the Poisson ratio are not required.

11

Figure 8 shows the phase differences for each excitation frequency for various Poissons ratios of $\nu = 0.45$, 0.40, 0.35, and 0.30. The values for $\nu = 0.30$ and 0.35 decrease with a small oscillation, but they do not cross the zero axis. This means that the synchronized frequency can not be defined for $\nu = 0.30$ and 0.35. Additionally, for $\nu = 0.40$, the proposed value $\tilde{I}_0 = 2.2788$ causes larger errors than in the other cases. This implies that the proposed approach is only ensured for the $\nu \geq 0.41$ cases.

The Poisson ratio of the soil skeleton is approximately in the range of 0.2–0.3 (Kokusho, 1980; Lade and Nelson, 1987; Nakagawa et al., 1997), whereas moist soil will give larger values. Yang and Sato (2000) describe the relation between the Poisson ratio and the degree of saturation, and almost saturated ground exhibits a higher Poisson ratio regardless of the other parameters. On the basis of the relation between the wave velocities and the Poisson ratio,

$$\frac{\alpha}{\beta} = \sqrt{\frac{2(1-\nu)}{1-2\nu}}, \tag{19}$$

$\nu \geq 0.41$ means that the P-wave velocity is larger than 2.56β, e.g., $\geq 256\,\mathrm{m/s}$ for a $100\,\mathrm{m/s}$ S-wave velocity, $\geq 1024\,\mathrm{m/s}$ for $400\,\mathrm{m/s}$, and so forth, which are almost satisfactory for a natural soil deposit. Therefore, the range of application is reasonable for our motivation to measure the S-wave impedance.

The main scope of this study is not to discuss the dynamic behaviors of the disk under actual earthquake ground motions but to measure the S-wave impedance of the soil material as one of the techniques of geophysical explorations. The excitation frequencies are not limited in the range of important frequencies for ground motions, e.g., 0.1–10.0 Hz. In fact, a simple pulse, mainly containing higher frequency components, is generally used in PS loggings and reflection surveys, whereas the material properties, the P and S-wave velocities, obtained from the surveys, are widely applied to geotechnical engineering applications.

4. Measurement procedure for the S-wave impedance

On the basis of the properties of the relation between the disk velocity and the reaction force acting on the rigid circular disk, we propose a simple procedure to measure the S-wave impedance of the uppermost layer of the surface ground.

Step 1. A rigid circular disk is vertically loaded at variable frequencies, and the reaction force and disk velocity are measured.

We set a rigid circular disk on the ground surface and vertically load it by sinusoidal wave excitation with a variety of frequencies (see Fig. 1). The reaction force acting on the disk and the disk velocity are measured for each frequency.

Step 2. The synchronized frequency between the reaction force and the disk velocity is determined.

The time series of the measured reaction force is compared to the one for the disk velocity (see Fig. 3), and their phase difference is caluculated. The excitation frequency with zero phase difference is then determined and set to the synchronized frequency (see the top panel of Fig. 4).

Step 3. The ratio of the averaged reaction pressure to the disk velocity at the synchronized frequency is calculated.

The amplitude of the averaged reaction pressure, which is defined by $P_z/\pi a^2$, is divided by the amplitude of the disk velocity at the synchronized frequency. The value is set to the measured ratio (see the bottom panel of Fig. 4).

Step 4. The ratio is divided by $\tilde{I}_0 = 2.2788$, and then, the S-wave impedance is obtained.

As shown in Fig. 5, the measured ratio divided by the material S-wave impedance is constant independent of the material properties, and it is modeled with the value of $\tilde{I}_0 = 2.2788$. Therefore, the measured ratio is divided by 2.2788, and we can then obtain the S-wave impedance of the uppermost surface layer at the target site.

If horizontal loadings to the circular disk are required in the procedure, we must ensure strong coupling to the contact surface to prevent slippage between

13

the disk and the ground surface. The procedure used here, fortunately, requires only vertical loadings to estimate the S-wave impedance. This allowed us to realize the loading system without having to implement special treatments to the contact surface.

The proposed procedure was verified in a homogeneous half-space medium, even though the natural ground surface cannot be assumed to be a homogeneous half-space. Therefore, in order to clarify the effects of the material interfaces and inhomogeneity, we demonstrate the measured procedure for more general media through two numerical experiments.

5. Numerical experiment 1: two-layered medium

We first clarify the effect of the material interfaces by performing numerical experiments on a two-layered medium, which consists of a single surface layer overlying a homogeneous half-space basement. The physical parameters of both the surface layer and basement are presented in Table 2. We evaluated three cases with variable surface layer thicknesses of $0.5\,\mathrm{m}$, $1.0\,\mathrm{m}$, and $2.0\,\mathrm{m}$ and the half-space case as a reference. The Poisson ratios of the surface layer and basement were 0.493 and 0.43, respectively, which are in the applicable range of $\tilde{I}_0 = 2.2788$.

For the half-space medium, the results were independent of the disk radius. However, for the two-layered medium, a relation between the disk radius and the surface layer thickness was apparent. We performed numerical experiments by applying seven disk radii for each case: $0.1\,\mathrm{m}$, $0.2\,\mathrm{m}$, $0.5\,\mathrm{m}$, $1.0\,\mathrm{m}$, $2.0\,\mathrm{m}$, $5.0\,\mathrm{m}$, and $10.0\,\mathrm{m}$. In order to ensure 50 elements beneath each disk size, the size of the elements was modified in each simulation of the disk radius. We then applied the proposed procedure described in the previous section to estimate the S-wave impedance. We omit the case for a disk radius of $0.1\,\mathrm{m}$ and a thickness of $2.0\,\mathrm{m}$ because the thickness exceeds the vertical dimension of the entire domain. For the other cases, the relative element sizes to the wavelength is ensured to be sufficiently small, e.g., 25 elements represent the wavelength at the synchronized

14

frequency for a disk radius of $10\,\mathrm{m}$ and a thickness of $0.5\,\mathrm{m}$.

Figure 9 shows the S-wave impedances estimated from the various disk radii. The black solid lines indicate the true S-wave impedances in the surface layer and basement. For small disk radii, namely, 0.1–$0.2\,\mathrm{m}$, the estimated S-wave impedances agreed well with the S-wave impedances of the surface layer. However, the values were underestimated at a radius of approximately $1\,\mathrm{m}$, and they increased to the S-wave impedance of the basement as the radius increased. Table 3 lists the synchronized frequencies for each case. The small disk size generates a wave field that mainly consists of shorter wavelengths at the syncchronized frequency. In one example, the wavelength for a disk radius of $0.2\,\mathrm{m}$ and a thickness of $1.0\,\mathrm{m}$ is $0.57\,\mathrm{m}$, which is half of the surface layer thickness. The table also implies that a wavelength shorter than the layer thickness gives almost the same synchronized frequencies as the half-space case. Therefore, the effect from the layer boundary depends on the relative size of the disk to the layer thickness.

To enhance the relative thickness to the disk radius, we plotted the estimated values associated with a normalized disk radius, which was defined by the disk radius divided by the surface layer thickness, in Fig. 10. This clearly shows that all cases are on a common curve, and the minimum value appears when the disk radius is equal to the surface layer thickness. This implies that the S-wave impedances estimated from approximately 20% size of the disk radius relative to the surface layer thickness must be correct. In general, we did not have much information about the layer thickness at the target site, but several experiments with a variety of disk radii will give a curve similar to that shown in Fig. 10, and this will give an appropriate value of the S-wave impedance as a limiting value for shorter disk sizes.

6. Numerical experiment 2: 1-D random medium

Natural materials that compose the ground surface usually have variable material properties. We performed another numerical experiment for more complex

15

layered structures in order to check the robustness of the proposed method.

The variations in velocities and densities were applied only to the depth direction, and they were modeled by adding fluctuations to the average model. Table 4 summarizes the parameters for the average model, which is based on 1-D profiles at the K-NET MYG006 seismic station maintained by the National Research Institute for Earth Science and Disaster Prevention (NIED). Severe residential damage around the K-NET MYG006 site was concentrated during the 2011 off the Pacific coast of Tohoku earthquake (Goto and Morikawa, 2012). The detailed soil profiles have been investigated from the very dense observations of strong ground motions (Goto et al., 2012), and the soft soil deposit is estimated to a depth of approximately 15–30 m. Although there are no significant reasons to adopt the profile at the K-NET MYG006 site in this study, we choose a target site covered with the soft soil deposit because large site amplification is expected.

We adopted the von Kármán autocorrelation function $R(z)$ and applied it to the fluctuations (Sato et al., 2012); the function is

$$R(z) = \frac{\varepsilon^2 2^{1-\kappa}}{\Gamma(\kappa)} \left(\frac{z}{a}\right)^\kappa K_\kappa \left(\frac{z}{a}\right), \tag{20}$$

where $\Gamma(\kappa)$ is the gamma function, and K_κ is the modified Bessel function of the second kind of order κ. ε^2 is the mean square fractional fluctuation. a is the correlation distance. In the experiments, a and κ were set to 10 m and 0.5, respectively. Two cases of ε^2, 0.02 and 0.1, were examined. Figures 11 and 12 show the S-wave velocity and density models for $\varepsilon^2 = 0.02$ and 0.1, respectively. We generated 10 samples and performed numerical experiments for each case.

A 0.2 m disk radius was applied, and we then obtained simulation results using the measurement procedure for the S-wave impedance. Figure 13 shows the estimated S-wave impedance from the 1-D random medium. The horizontal axis corresponds to the sample number of the random model. Because the S-wave impedance of surface layer #1 contains fluctuations, the ranges of the standard deviation and minimum–maximum values are also plotted in Fig. 13. All estimated values were in the range of the minimum–maximum values of the

model for $\varepsilon^2 = 0.02$, and almost all of the cases were in the range of the standard deviation. For the strong fluctuation case ($\varepsilon^2 = 0.1$), the estimated value for one of the samples (sample 4) was outside the range of the minimum–maximum values. However, the estimates for over half of the cases were in the range of the standard deviation. This implies that the proposed method gives accurate estimates of the S-wave impedance of the uppermost surface layer, even when the material includes some fluctuations.

7. Conclusion

In this study, we proposed a new approach to measure the S-wave impedance in the uppermost surface layer. A rigid circular disk is set on a free surface, and it vertically oscillates as it synchronizes with the reaction force and disk velocity. The ratio of the averaged reaction pressure to the velocity is a product of the S-wave impedance and a coefficient estimated as $\tilde{I}_0 = 2.2788$. The S-wave impedance estimated from the procedure is quite accurate in numerical experiments for a homogeneous half-space medium. For the two-layered medium, the estimated value is appropriate when a small disk radius is selected. For the 1-D random medium, the proposed approach gives accurate estimates compared to the variation itself.

References

Aki, K., 1957. Space and time spectra of stationary stochastic waves, with special reference to microtremors. Bull. Earthquake Res. Inst., University of Tokyo 35, 415–456.

Aki, K., 1965. A note on the use of microseisms in determining the shallow structure of the earth's crust. Geophysics 30, 665–666. doi:`10.1190/1.1439640`.

Allen, S.J., 1980. Seismic method. Geophysics 45, 1619–1633. doi:`10.1190/1.1441053`.

Allen, T.I., Wald, D.J., 2009. On the use of high-resolution topographic data as a proxy for seismic site conditions (VS30). Bull. Seism. Soc. Am. 99, 935–943. doi:`10.1785/0120080255`.

Boore, D.M., 2006. Determining subsurface shear-wave velocities: a review, in: Proc. of 3rd International Symposium on the Effects of Surface Geology on Seismic Motion.

Boore, D.M., Thompson, E.M., 2007. On using surface-source downhole-receiver logging to determine seismic slownesses. Soil Dyn. Earthquake Eng. 27, 971–985. doi:`10.1016/j.soildyn.2007.03.005`.

Borcherdt, R.D., 1994. Estimates of site–dependent response spectra for design (methodology and justification). Earthquake Spectra 10, 617–653. doi:`10.1193/1.1585791`.

Boussinesq, J.V., 1885. Application des potentiels l'tude de l'quilibre et du mouvement des solides lastiques. Gauthier-Villars.

Bouzorgnia, Y., Bertero, V.V., 2004. Earthquake Engineering from Engineering Seismology to Performance-Based Engineering. CRC Press.

Castellaro, S., Mulargia, F., Rossi, P.L., 2008. Vs30: Proxy for seismic amplification? Seism. Res. Lett. 79, 540–543. doi:`10.1785/gssrl.79.4.540`.

Connolly, P., 1999. Elastic impedance. The Leading Edge 18, 438–452. doi:`10.1190/1.1438307`.

Gazetas, G., 1991. Formulas and charts for impedances of surface and embedded foundations. J. Geotech. Engrg. 117, 1363–1381. doi:`10.1061/(ASCE)0733-9410(1991)117:9(1363)`.

Gazetas, G., Dobry, R., 1984. Simple radiation damping model for piles and footings. J. Eng. Mech. 110, 937–956. doi:`10.1061/(ASCE)0733-9399(1984)110:6(937)`.

Gazetas, G., Tassoulas, J.L., 1987. Horizontal damping of arbitrarily shaped embedded foundations. J. Geotech. Engrg. 113, 458–475. doi:`10.1061/(ASCE)0733-9410(1987)113:5(458)`.

Gerolymos, N., Gazetas, G., 2006. Winkler model for lateral response of rigid caisson foundations in linear soil. Soil Dyn. Earthquake Eng. 26, 347–361. doi:`10.1016/j.soildyn.2005.12.003`.

Goto, H., Kawamura, Y., Sawada, S., Akazawa, T., 2013. Direct estimation of near-surface damping based on normalized energy density. Geophys. J. Int. 194, 488–498. doi:`10.1093/gji/ggt104`.

Goto, H., Morikawa, H., 2012. Ground motion characteristics during the 2011 off the Pacific coast of Tohoku earthquake. Soils and Foundations 52, 769–779. doi:`10.1016/j.sandf.2012.11.002`.

Goto, H., Morikawa, H., Inatani, M., Ogura, Y., Tokue, S., Zhang, X., Iwasaki, M., Araki, M., Sawada, S., Zerva, A., 2012. Very dense seismic array observations in Furukawa district, Japan. Seism. Res. Lett. 83, 765–774. doi:`10.1785/0220120044`.

Goto, H., Sawada, S., Hirai, T., 2011. Conserved quantity of elastic waves in multi-layered media: 2D SH case –Normalized Energy Density–. Wave Motion 48, 603–613. doi:`10.1016/j.wavemoti.2011.04.011`.

Goto, H., Takahashi, C., Ishii, Y., Ling, S.Q., Miyakoshi, K., Morikawa, H., Sato, Y., Sawada, S., Shingaki, Y., Suzuki, Y., Takabatake, D., Joshima, M., 2009. Deep subsurface structure estimated by microtremors array observations and gravity surveys in Kashiwazaki area, Japan. Soils and Foundations 49, 651–659. doi:`10.3208/sandf.49.651`.

Hata, Y., Ichii, K., Nozu, A., Maruyama, Y., Sakai, H., 2014. Evaluation of strong ground motion at Imagawa, Urayasu city, during the 2011 off the Pacific coast of Tohoku earthquake. Soils and Foundations 54, 573–587. doi:`10.1016/j.sandf.2014.06.003`.

Jia, R., Hino, T., Chai, J., Hamada, T., Yoshimura, M., 2013. Interpretation of density profile of seabed sediment from nuclear density cone penetration test results. Soils and Foundations 53, 671–679. doi:`10.1016/j.sandf.2013.08.005`.

Joyner, W.B., Warrick, R.E., Fumal, T.E., 1981. The effect of quanternary alluvium on strong ground motion in the Coyote lake, California, earthquake of 1979. Bull. Seism. Soc. Am. 71, 1333–1349.

Kausel, E., 2010. Early history of soil-structure interaction. Soil Dyn. Earthquake Eng. 30, 822–832. doi:`10.1016/j.soildyn.2009.11.001`.

Kokusho, T., 1980. Cyclic triaxial test of dynamic soil properties for wide strain range. Soils and Foundations 20, 45–60.

Lade, P.V., Nelson, R.B., 1987. Modelling the elastic behaviour of granular materials. Int. J. Num. Anal. Methods Geomech. 11, 521–542. doi:`10.1002/nag.1610110507`.

Lamb, H., 1902. On Boussinesq's problem. Proc. London Math. Soc. 34, 276–284.

Lee, V.W., Trifunac, M.D., 2010. Should average shear-wave velocity in the top 30 m of soil be used to describe seismic amplification? Soil Dyn. Earthquake Eng. 30, 1250–1258. doi:`10.1016/j.soildyn.2010.05.007`.

Liu, H.P., Boore, D.M., Joyner, W.B., Oppenheimer, D.H., Warrick, R.E., Zhang, W., Hamilton, J.C., Brown, L.T., 2000. Comparison of phase velocities from array measurements of Rayleigh waves associated with microtremor and results calculated from borehole shear-wave velocity profiles. Bull. Seism. Soc. Am. 90, 666–678. doi:`10.1785/0119980186`.

Lu, S., McMechan, G.A., 2004. Elastic impedance inversion of multichannel seismic data from unconsolidated sediments containing gas hydrate and free gas. Geophysics 69, 164–179. doi:10.1190/1.1649385.

Mori, T., Tobita, Y., Okimura, T., 2012. The damage to hillside embankments in Sendai city during the 2011 off the Pacific coast of Tohoku earthquake. Soils and Foundations 52, 910–928. doi:10.1016/j.sandf.2012.11.011.

Nakagawa, K., Soga, K., Mitchell, J.K., 1997. Observation of Biot compressional wave of the second kind in granular soils. Geotechnique 47, 133–147. doi:10.1680/geot.1997.47.1.133.

Okada, H., 2003. The Microtremor Survey Method. Society of Exploration Geophysicists.

Park, C.B., Miller, R.D., Xia, J., 1999. Multichannel analysis of surface waves. Geophysics 64, 800–808. doi:10.1190/1.1444590.

Robertson, I.A., 1966. Forced vertical vibration of a rigid circular disc on a semi-infinite elastic solid. Math. Proc. Camb. Phil. Soc. 62, 547–553. doi:10.1017/S0305004100040184.

Sato, H., Fehler, M.C., Maeda, T., 2012. Seismic Wave Propagation and Scattering in the Heterogeneous Earth: Second Edition. Springer.

Seed, H.B., Idriss, I.M., 1971. Simplified procedure for evaluating soil liquefaction potential. J. Soil Mech. Found. Div., ASCE 97, 1249–1273.

Sugano, T., Nozu, A., Kohama, E., ichiro Shimosako, K., Kikuchi, Y., 2014. Damage to coastal structures. Soils and Foundations 54, 883–901. doi:10.1016/j.sandf.2014.06.018.

Thompson, E.M., Wald, D.J., Worden, C.B., 2014. A VS30 map for California with geologic and topographic constraints. Bull. Seism. Soc. Am. 104, 2313–2321. doi:10.1785/0120130312.

Towhata, I., Maruyama, S., ichi Kasuda, K., Koseki, J., Wakamatsu, K., Kiku, H., Kiyota, T., Yasuda, S., Taguchi, Y., Aoyama, S., Hayashida, T., 2014. Liquefaction in the Kanto region during the 2011 off the Pacific coast of Tohoku earthquake. Soils and Foundations 54, 859–873. doi:10.1016/j.sandf.2014.06.016.

Unjoh, S., Kaneko, M., Kataoka, S., Nagaya, K., Matsuoka, K., 2012. Effect of earthquake ground motions on soil liquefaction. Soils and Foundations 52, 830–841. doi:10.1016/j.sandf.2012.11.006.

Wakamatsu, K., Matsuoka, M., 2006. Development of the 7.5-arc-second engineering geomorphologic classification database and its application to seismic microzoning. Bull. Earthquake Res. Inst., University of Tokyo 81, 317–324.

Wald, D.J., Allen, T.I., 2007. Topographic slope as a proxy for seismic site conditions and amplification. Bull. Seism. Soc. Am. 97, 1379–1395. doi:10.1785/0120060267.

Wald, D.J., Jaiswal, K.S., Marano, K.D., Bausch, D.B., Hearne, M.G., 2010. PAGER–Rapid assessment of an earthquake's impact. U.S. Geological Survey Fact Sheet 2010-3036.

Whitcombe, D.N., 2002. Elastic impedance normalization. Geophysics 67, 60–62. doi:10.1190/1.1451331.

Wolf, J.P., 1997. Spring-dashpot-mass models for foundation vibrations. Earth. Eng. Struct. Dyn. 26, 931–949. doi:10.1002/(SICI)1096-9845(199709)26:9.

Wolf, J.P., Somaini, D.R., 1986. Approximate dynamic model of embedded foundation in time domain. Earth. Eng. Struct. Dyn. 14, 683–703. doi:10.1002/eqe.4290140502.

Yang, J., Sato, T., 2000. Interpretation of seismic vertical amplification observed at an array site. Bull. Seism. Soc. Am. 90, 275–285. doi:10.1785/0119990068.

Yasuda, S., Harada, K., Ishikawa, K., Kanemaru, Y., 2012. Characteristics of liquefaction in Tokyo bay area by the 2011 Great East Japan earthquake. Soils and Foundations 52, 793–810. doi:`10.1016/j.sandf.2012.11.004`.

Yokokura, T., 1995. Research and development on the multi-channel seismic reflection method and its applications to various geological situations in Japan. J. Phys. Earth 43, 321–349. doi:`10.4294/jpe1952.43.321`.

Table 1: Physical parameters of the homogeneous half-space medium. All ombinations (140 cases) are numerically simulated.

S-wave velocity [m/s]	100, 200, 300, 400, 500, 600, 700, 800, 900, 1000
Density [kg/m^3]	1500, 2000
Poisson ratio	0.40, 0.41, 0.43, 0.45, 0.47, 0.48, 0.49

Table 2: Physical parameters for the two-layered medium.

	Surface layer	Basement
S-wave velocity [m/s]	180	700
P-wave velocity [m/s]	1500	2000
Density [kg/m^3]	1400	1600
Thickness [m]	0.5, 1.0, 2.0, ∞	–

Table 3: Synchronized frequencies for the two-layered medium. The symbol * indicates that the corresponding wavelength is shorter than the layer thickness.

	Disk radius [m]						
Thickness [m]	0.1	0.2	0.5	1.0	2.0	5.0	10.0
0.5	*630 Hz	225 Hz	183 Hz	180 Hz	185 Hz	95 Hz	36 Hz
1.0	*647 Hz	*315 Hz	102 Hz	92 Hz	90 Hz	97 Hz	48 Hz
2.0	–	*323 Hz	*132 Hz	51 Hz	46 Hz	46 Hz	49 Hz
∞	*645 Hz	*323 Hz	*129 Hz	*65 Hz	*32 Hz	*13 Hz	6.5 Hz

Table 4: Average model for the one-dimensional (1-D) random medium. Each physical parameter is based on 1-D profiles at the K-NET MYG006 seismic station maintained by the National Research Institute for Earth Science and Disaster Prevention (NIED).

	Surface layer #1	Surface layer #2	Basement
S-wave velocity [m/s]	70	130	400
P-wave velocity [m/s]	350	1420	1880
Density [kg/m^3]	1425	1750	2110
Thickness [m]	2.0	15.0	–
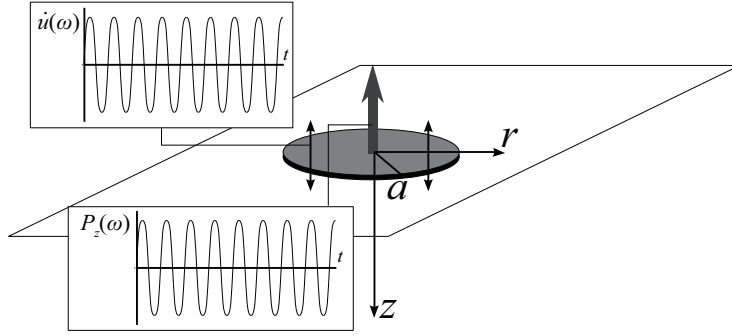
Figure 1: Schematic of a rigid circular disk vertically loaded by sinusoidal wave excitation. The disk velocity $\dot{u}(\omega)$ and the reaction force from the ground surface $P_z(\omega)$ are measured values. r and z are the axes of the cylindrical coordinate system that are prallel to the disk radius and depth directions, respectively.
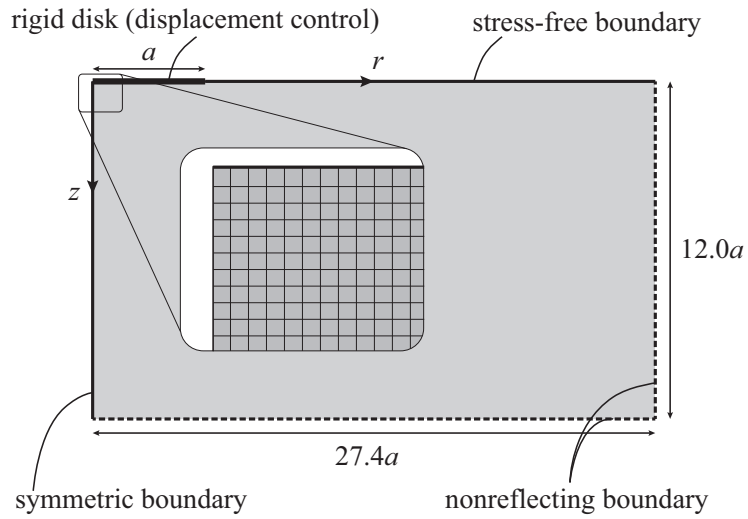
Figure 2: Finite element model of the cylindrical coordinate system with axial symmetry for the numerical experiments. The rigid circular disk is modeled by the displacement boundary condition.
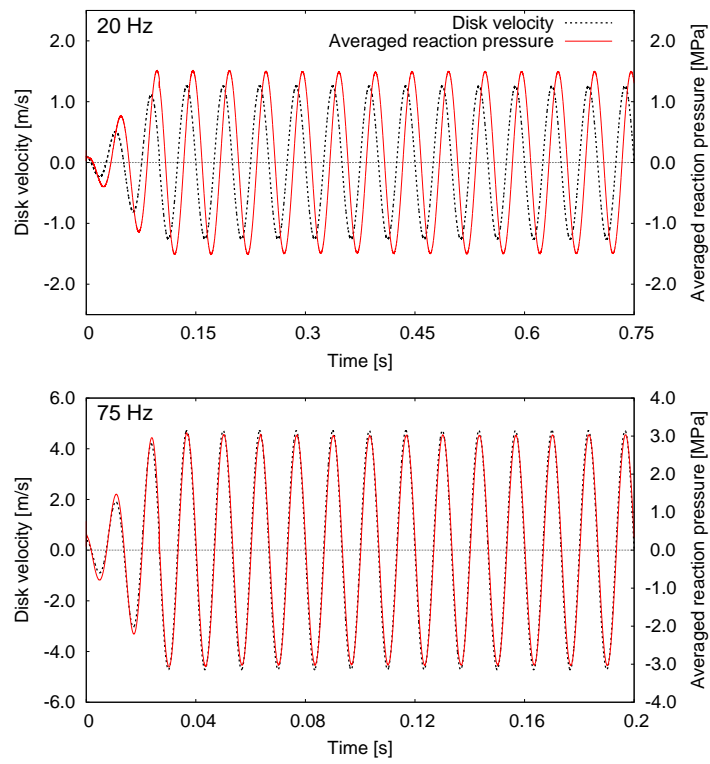
Figure 3: Comparison between the disk velocity and the average reaction pressure on the disk for $\beta = 200 \, \text{m/s}$, $\rho = 1500 \, \text{kg/m}^3$, and $\nu = 0.45$.
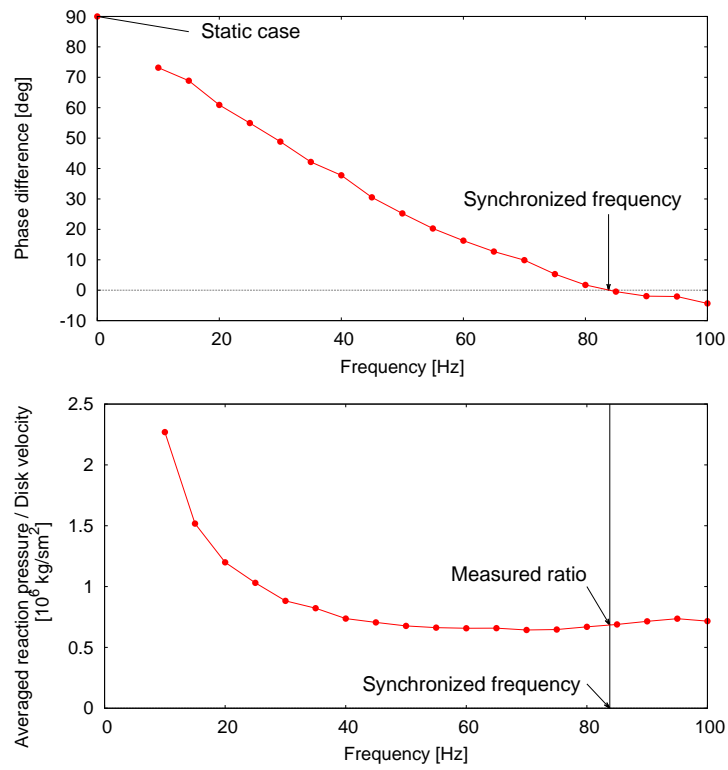
Figure 4: Phase differences and the ratio of the average reaction force to the disk velocity depending on the excitation frequency for $\beta = 200\,\mathrm{m/s}$, $\rho = 1500\,\mathrm{kg/m^3}$, and $\nu = 0.45$.
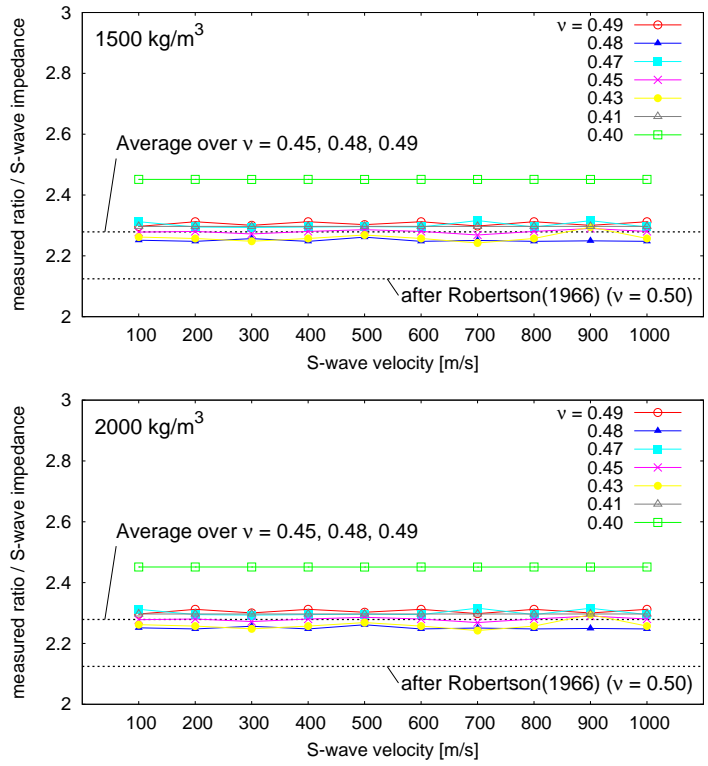
Figure 5: The ratio of the measured ratio to the material S-wave impedance $(\tilde{I}_0)$ for all cases.
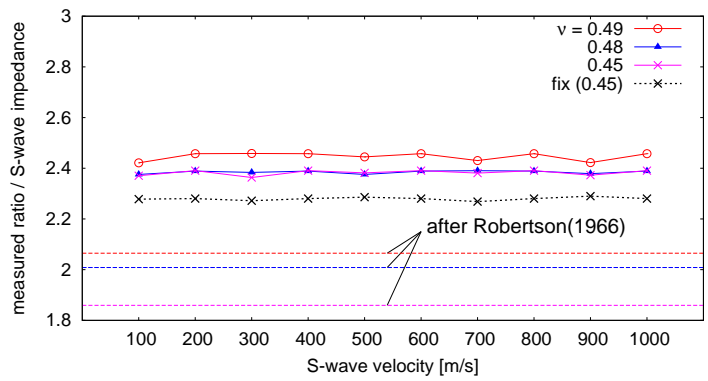
Figure 6: The ratio of the measured ratio to the material S-wave impedance for the cases allowing frictionless sliding between the disk and the ground surface.
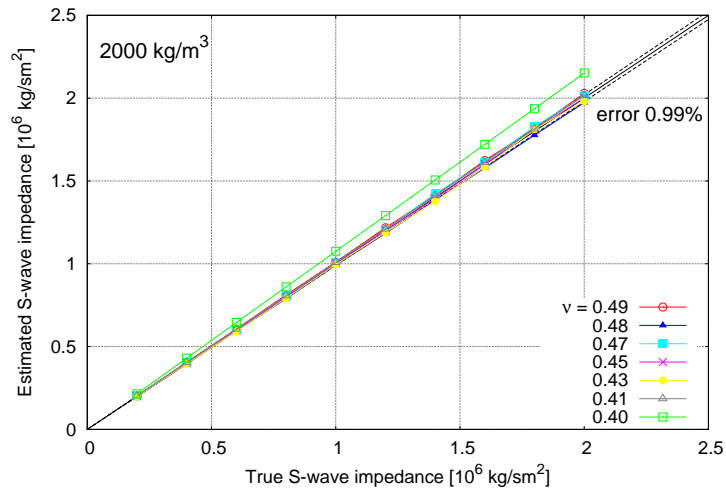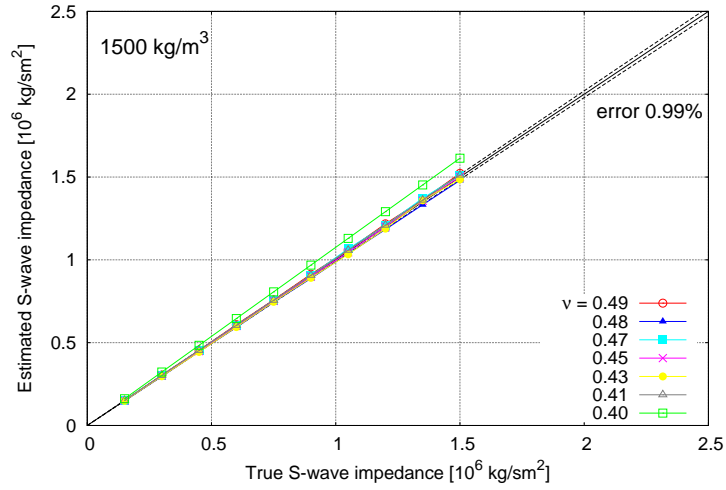
Figure 7: Comparison of the estimated S-wave impedance to the material (true) one by using the coefficient $\tilde{I}_0 = 2.2788$.
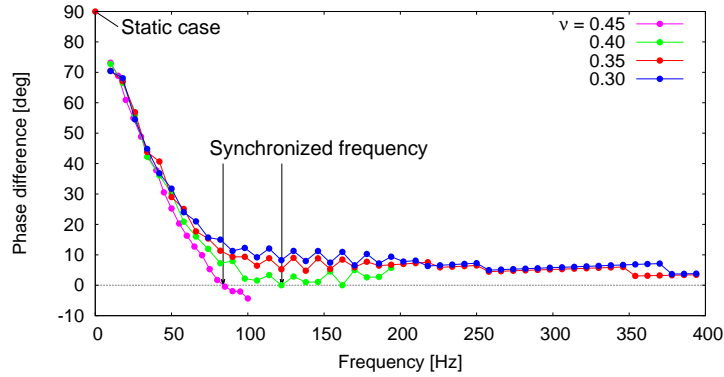
Figure 8: Examples of phase differences depending on the excitation frequency for $\nu = 0.45$, 0.40, 0.35, and 0.30 ($\beta = 200\,\mathrm{m/s}$, $\rho = 1500\,\mathrm{kg/m^3}$).
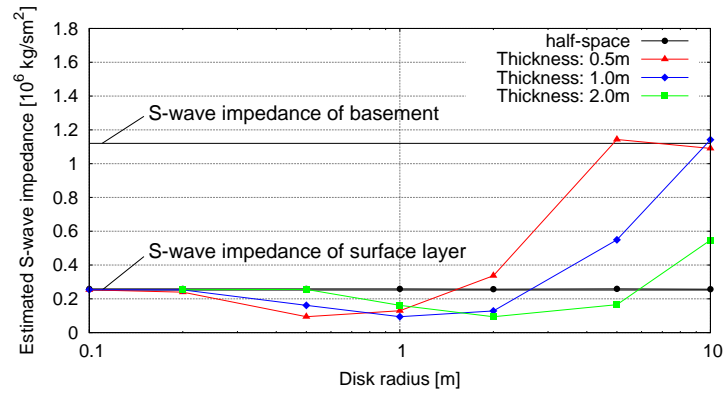
Figure 9: Estimated S-wave impedance depending on the disk radius for the two-layered medium. Black solid lines indicate the true S-wave impedances in the surface layer and basement.
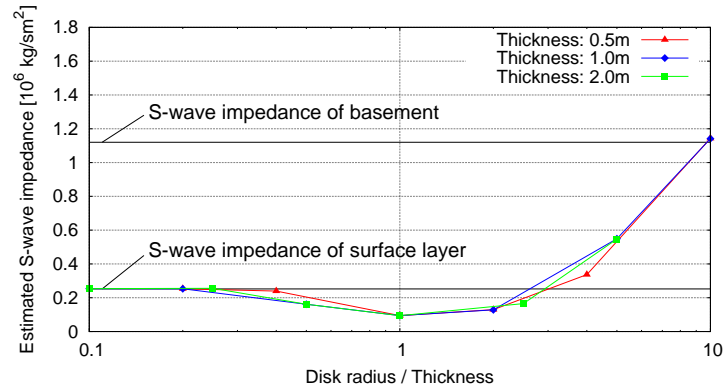
Figure 10: Estimated S-wave impedance for the two-layered medium plotted with a normalized disk radius, which was defined by the disk radius divided by the surface layer thickness.
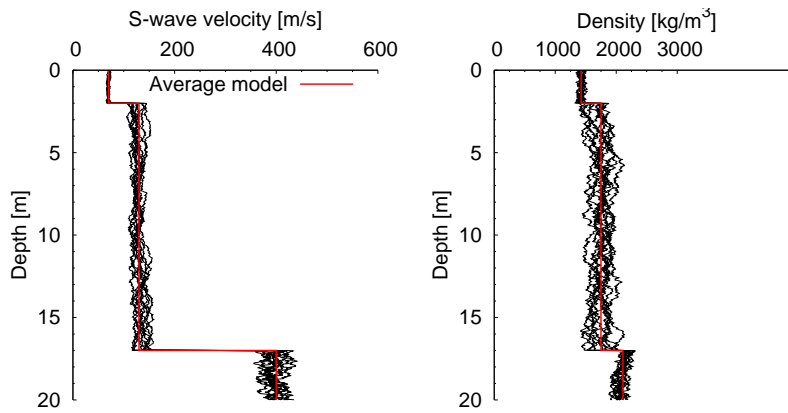

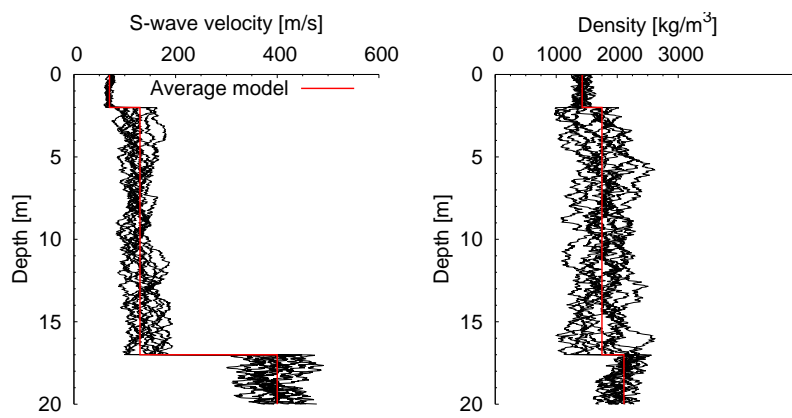Figure 11: Ten random models for the S-wave velocity and density ($\varepsilon^2 = 0.02$).

31

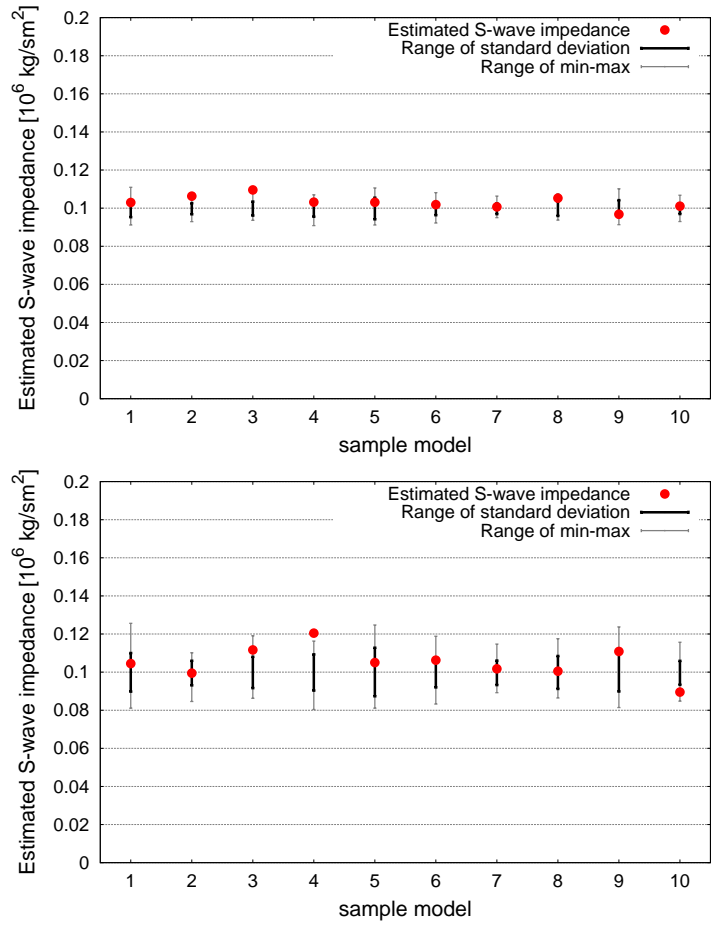Figure 12: Ten random models for the S-wave velocity and density ($\varepsilon^2 = 0.1$).

Figure 13: Estimated S-wave impedances for each of the 10 sample models. Black and gray ranges indicate the ranges of the standard deviation and minimum–maximum values for the uppermost surface layers in the models (top: $\varepsilon^2 = 0.02$, bottom: $\varepsilon^2 = 0.1$).